PHYSICAL REVIEW A **108**, 033520 (2023)

Multimode perturbation modeling for cavity polygon and star modes

Saeed Farajollahi,[1] Zhiwei Fang,[2] Jintian Lin,[3,4] Shahin Honari,[1] Ya Cheng,[2,3,4,5,6,7,*] and Tao Lu[1,†]
[1]*Department of Electrical and Computer Engineering, University of Victoria, Victoria, British Columbia, Canada, V8P 5C2*
[2]*XXL—The Extreme Optoelectromechanics Laboratory, School of Physics and Electronic Science, East China Normal University, Shanghai 200241, China*
[3]*State Key Laboratory of High Field Laser Physics and CAS Center for Excellence in Ultra-Intense Laser Science, Shanghai Institute of Optics and Fine Mechanics (SIOM), Chinese Academy of Sciences (CAS), Shanghai 201800, China*
[4]*Center of Materials Science and Optoelectronics Engineering, University of Chinese Academy of Sciences, Beijing 100049, China*
[5]*State Key Laboratory of Precision Spectroscopy, East China Normal University, Shanghai 200062, China*
[6]*Collaborative Innovation Center of Extreme Optics, Shanxi University, Taiyuan 030006, China*
[7]*Collaborative Innovation Center of Light Manipulations and Applications, Shandong Normal University, Jinan 250358, China*

(Received 17 April 2023; accepted 11 September 2023; published 26 September 2023)

Polygon and star modes enable unidirectional emission and single-frequency lasing in whispering gallery microcavities. To understand their properties and facilitate design, we have adopted both two-dimensional and three-dimensional full-wave perturbation methods to simulate these modes. Our simulation demonstrates that a tapered optical fiber can be used as a weak perturbation to coherently combine multiple whispering gallery modes into a polygon or star mode. Additionally, our simulation predicts an optical quality factor as high as 10^7 for the polygon modes, which is in good agreement with the experimental results.

DOI: 10.1103/PhysRevA.108.033520

I. INTRODUCTION

Conventional optical whispering gallery microresonators are known for their high-quality factors (Q) and small mode volume, making them suitable candidates for a range of applications from sensing, frequency microcomb generation, quantum information, to optomechanics [1–7]. When the azimuthal symmetry is lifted through structural deformation, a whispering gallery microcavity may form chaotic modes that evolve to star or polygon modes under certain conditions. In the past, intriguing phenomena such as unidirectional emission have been found in these cavities [8–13]. However, due to large optical loss arising from deformation, the high quality factor needed for activating nonlinear optical effects does not materialize. Recently, these modes were observed in lithium niobate (LN) microdisks for which the azimuthal symmetry is lifted through a weak perturbation from a tapered optical fiber [14,15]. In contrast to deformed whispering gallery microresonators, these microdisks can have polygon and star modes without degrading Q. Hence, they can be used in novel applications such as second harmonic generation, optomechanical oscillation, and frequency microcomb generation due to the high intracavity optical intensity.

For deformed cavities, the formation of these modes has been explained by describing internal ray dynamics using the Poincaré surface of a section [8–13]. However, obtaining a full vector, three-dimensional (3-D) field profile, resonance wavelength, and quality factor of these modes remains a challenge. One way to obtain these parameters is to perform full wave first-principle-based 3-D simulations on the structure. However, such a 3-D simulation of nonsymmetric microcavities is computationally intensive. To accommodate this issue, two-dimensional (2-D) approximations such as effective index methods (see details in Supplemental Material, Sec. S.1 [16]) are often applied [14,15,17–20]. Although proven to be powerful for photonic structures with low refractive index contrast profile, such approximation yields large inaccuracy in the case of microcavity simulation due to the large refractive index difference between the cavity material and ambient air.

In the past, perturbation methods were used as a powerful tool for chaotic mode analysis in microcavities [21–25]. In those implementations, the field profile of a whispering gallery microcavity having structural deformation or in the presence of a perturbed object was represented as a linear superposition of ideal whispering gallery modes (WGMs) field profile whose resonance wavelengths are close to the probe laser wavelength [26,27] and nonzero superposition coefficients are only available at a discrete number of resonant wavelengths [27–29]. At certain wavelengths, different polygon and star modes can be formed.

In this paper, through first-order perturbation, we investigate the formation of polygon and star modes in fiber-perturbed cavities. In contrast to the previous formalisms [27–29], we adopt a nonintegral azimuthal mode order of each WGM to improve the phase estimation accuracy. In addition to obtaining the field profile and resonance wavelength, we also formulate a robust algorithm for quality factor estimation [15,30].

---

[*] ya.cheng@siom.ac.cn

[†] taolu@ece.uvic.ca

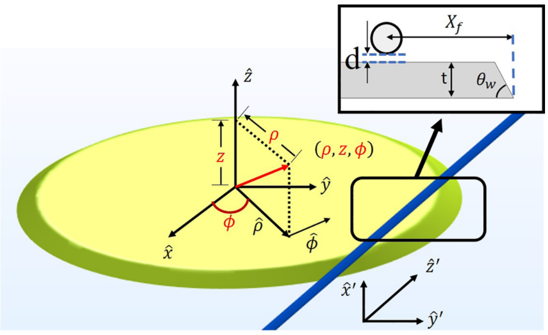

FIG. 1. Structure of a microdisk with radius R, thickness t, and wedge angle θ_w and a tapered fiber being placed on top of it. The vertical gap between the fiber and the microdisk top surface is denoted by d.

II. MULTIMODE PERTURBATION FORMALISM

The photonic device to be studied is shown in Fig. 1. Here, a tapered fiber is placed near an azimuthal-symmetric z-cut LN microdisk with radius R, thickness t, and wedge angle θ_w, along $\hat{x}$; all are labeled in Fig. 1. The vertical gap between the fiber and the top surface of the disk is defined as d. X_f is the horizontal distance from the center of the fiber to the bottom edge of the microdisk at $\phi = \frac{\pi}{2}$ according to current settings. Here a negative X_f represents the fiber being placed on top of the microdisk.

The multimode perturbation formalism starts with the Helmhöltz equations that characterize the electric $\vec{E}(\rho, z, \phi)$ and magnetic $\vec{H}(\rho, z, \phi)$ field distributions of a nonmagnetic photonic structure with relative permittivity profile $\epsilon_r(\rho, z, \phi)$,

$$\nabla^2 \vec{E}(\rho, z, \phi) + \epsilon_r(\rho, z, \phi) k_0^2 \vec{E}(\rho, z, \phi) = \vec{0},$$
$$\nabla^2 \vec{H}(\rho, z, \phi) + \epsilon_r(\rho, z, \phi) k_0^2 \vec{H}(\rho, z, \phi) = \vec{0}. \tag{1}$$

Here, in a cylindrical coordinates $(\hat{\rho}, \hat{z}, \hat{\phi})$ specified in Fig. 1, the second-order differential operator $\nabla^2 \equiv \frac{1}{\rho}\frac{\partial}{\partial \rho}(\rho \frac{\partial}{\partial \rho}) + \frac{1}{\rho^2}\frac{\partial^2}{\partial \phi^2} + \frac{\partial^2}{\partial z^2}$. $k_0 = \frac{2\pi}{\lambda_0}$ is the free-space wave number and λ_0 the vacuum wavelength of the probe laser. By definition, an ideal whispering gallery microcavity has an azimuthal independent relative permittivity profile $\epsilon_r(\rho, z, \phi) = \epsilon_r(\rho, z)$. Through the separation of variables between ϕ and (ρ, z), one may find a discrete set of resonance wavelengths $\lambda_0 \in \{\lambda_{\nu\mu}; \nu, \mu = 1, 2, \ldots, \}$ that lead to nonzero solutions $\vec{E}_{\nu\mu}(\rho, z, \phi)$ and $\vec{H}_{\nu\mu}(\rho, z, \phi)$ to the Helmhöltz equations, which are called whispering gallery modes (WGMs) in the form of

$$\vec{E}_{\nu\mu}(\rho, z, \phi) = \hat{e}_{\nu\mu}(\rho, z) e^{-jm_{\nu\mu}\phi},$$
$$\vec{H}_{\nu\mu}(\rho, z, \phi) = \hat{h}_{\nu\mu}(\rho, z) e^{-jm_{\nu\mu}\phi}. \tag{2}$$

Here, the integer subscripts (ν, μ) represent the azimuthal and transverse mode order, respectively. $m_{\nu\mu}$ is a complex number whose real part $\mathrm{Re}\{m_{\nu\mu}\} = \nu$ is equal to the azimuthal mode order to satisfy the single value condition $\vec{E}_{\nu\mu}(\rho, \phi, z) \approx \vec{E}_{\nu\mu}(\rho, \phi + 2\pi, z)$ when neglecting the optical losses. The imaginary part $\mathrm{Im}\{m_{\nu\mu}\}$ characterizes the loss and is related to the optical quality factor Q according to $Q = \frac{\mathrm{Re}\{m_{\nu\mu}\}}{2\mathrm{Im}\{m_{\nu\mu}\}}$. $\hat{e}_{\nu\mu}(\rho, z)$ and $\hat{h}_{\nu\mu}(\rho, z)$ are the electric and magnetic mode field distributions at transverse cross section that satisfy the ϕ-independent mode equations

$$\nabla_\perp^2 \hat{e}_{\nu\mu}(\rho, z) + \left[\epsilon_r(\rho, z) k_{\nu\mu}^2 - \frac{m_{\nu\mu}^2}{\rho^2}\right] \hat{e}_{\nu\mu}(\rho, z) = \vec{0},$$
$$\nabla_\perp^2 \hat{h}_{\nu\mu}(\rho, z) + \left[\epsilon_r(\rho, z) k_{\nu\mu}^2 - \frac{m_{\nu\mu}^2}{\rho^2}\right] \hat{h}_{\nu\mu}(\rho, z) = \vec{0}, \tag{3}$$

with $\nabla_\perp^2 \equiv \frac{1}{\rho}\frac{\partial}{\partial \rho}(\rho \frac{\partial}{\partial \rho}) + \frac{\partial^2}{\partial z^2}$ and $k_{\nu\mu} = \frac{2\pi}{\lambda_{\nu\mu}}$. When $\mathrm{Im}\{m_{\nu\mu}\}$ is sufficiently small, WGMs are quasi-orthogonal and $\hat{e}_{\nu\mu}(\rho, z)$ and $\hat{h}_{\nu\mu}(\rho, z)$ are normalized such that

$$\pi \epsilon_0 \iint \epsilon_r(\rho, z) \hat{e}_{\nu'\mu'}^* \cdot \hat{e}_{\nu\mu} \rho \, d\rho \, dz = \delta_{\nu\nu'} \delta_{\mu\mu'}, \tag{4}$$

with δ being the Kronecker delta. When a perturbation element such as a tapered fiber is placed in close proximity to the cavity, the relative permittivity becomes azimuthal dependent by a small amount $[\Delta\epsilon_r(\rho, z, \phi) \ll \epsilon_r(\rho, z)]$. A probe laser light at a wavelength λ_l and wave number $k_l = \frac{2\pi}{\lambda_l}$ delivered to the cavity through the tapered fiber may distribute its energy to several WGMs coherently. Therefore, the field around the cavity can be expressed as

$$\vec{E}(\rho, z, \phi) = \sum_{\nu,\mu} a_{\nu\mu} \hat{e}_{\nu\mu}(\rho, z) e^{-jm'_{\nu\mu}\phi},$$
$$\vec{H}(\rho, z, \phi) = \sum_{\nu,\mu} a_{\nu\mu} \hat{h}_{\nu\mu}(\rho, z) e^{-jm'_{\nu\mu}\phi}, \tag{5}$$

with the summation over N whispering gallery modes whose resonance wavelengths $\lambda_{\nu\mu}$ are close to λ_l. By assuming photons at both wavelengths, $\lambda_{\nu\mu}$ and λ_l travel at the same optical path length and experience the same optical loss, we obtain [31,32]

$$\mathrm{Re}\{m'_{\nu\mu}\} = \frac{\lambda_{\nu\mu}}{\lambda_l} \nu,$$
$$\mathrm{Im}\{m'_{\nu\mu}\} = \mathrm{Im}\{m_{\nu\mu}\}. \tag{6}$$

Unlike in [27] where the azimuthal mode number for WGMs in Eq. (5) does not change with wavelength, here we modify it to reduce the phase error. Substituting Eq. (5) into Eq. (1), we obtain

$$\nabla^2 \sum_{\nu\mu} a_{\nu\mu} \hat{e}_{\nu\mu}(\rho, z) e^{-jm'_{\nu\mu}\phi} + [\epsilon_r(\rho, z) + \Delta\epsilon_r(\rho, z, \phi)]$$
$$\times k_l^2 \sum_{\nu\mu} a_{\nu\mu} \hat{e}_{\nu\mu}(\rho, z) e^{-jm'_{\nu\mu}\phi} = \vec{0}. \tag{7}$$

For simplicity, we relabel subscripts (ν, μ) with a single integer $(\gamma; \gamma \in 1, 2, \ldots, N)$, replace all subscript pairs accordingly, and define Δk_γ and Δm_γ according to

$$k_l = k_\gamma + \Delta k_\gamma,$$
$$m'_\gamma = m_\gamma + \Delta m_\gamma. \tag{8}$$

Following the perturbation approximation, we keep the first-order perturbation terms and neglect all higher-order terms and obtain

$$\sum_{\gamma} a_{\gamma}\left\{\nabla_{\perp}^{2}\hat{e}_{\gamma}(\rho,z)+\left[\epsilon_{r}(\rho,z)k_{\gamma}^{2}-\frac{m_{\gamma}^{2}}{\rho^{2}}\right]\hat{e}_{\gamma}(\rho,z)\right.$$
$$+\left[2\epsilon_{r}(\rho,z)k_{\gamma}\Delta k_{\gamma}+k_{\gamma}^{2}\Delta\epsilon_{r}(\rho,z,\phi)-\frac{2m_{\gamma}\Delta m_{\gamma}}{\rho^{2}}\right]$$
$$\left.\times\,\hat{e}_{\gamma}(\rho,z)\right\}e^{-jm'_{\gamma}\phi}=\vec{0}. \tag{9}$$

Since the first two terms on the left side of the equation vanish according to Eq. (3), we have

$$\sum_{\gamma} a_{\gamma}\left[2\epsilon_{r}(\rho,z)k_{\gamma}\Delta k_{\gamma}+k_{\gamma}^{2}\Delta\epsilon_{r}(\rho,z,\phi)-\frac{2m_{\gamma}\Delta m_{\mu}}{\rho^{2}}\right]$$
$$\times\,\hat{e}_{\gamma}(\rho,z)e^{-jm'_{\gamma}\phi}=\vec{0}. \tag{10}$$

Finally, multiplying the remaining terms by $\{\hat{e}^{*}_{\gamma'}(\rho,z)e^{jm'_{\gamma'}\phi};\gamma'\in 1,2,\ldots,N\}$ and integrating over full space, we get N homogeneous linear equations with N unknowns, which can be expressed in a matrix form

$$\tilde{\Lambda}(\lambda_{l})\vec{a}=\begin{bmatrix}\Lambda_{11} & \ldots & \Lambda_{1N}\\ \vdots & \ddots & \vdots\\ \Lambda_{N1} & \ldots & \Lambda_{NN}\end{bmatrix}\begin{bmatrix}a_{1}\\ \vdots\\ a_{N}\end{bmatrix}=\begin{bmatrix}0\\ \vdots\\ 0\end{bmatrix}. \tag{11}$$

Here, the matrix element $\Lambda_{\gamma'\gamma}(\lambda_{l})$ is λ_{l} dependent

$$\Lambda_{\gamma'\gamma}(\lambda_{l})$$
$$=\iiint\left[2\epsilon_{r}(\rho,z)k_{\gamma}\Delta k_{\gamma}+k_{\gamma}^{2}\Delta\epsilon_{r}(\rho,z,\phi)-\frac{2m_{\gamma}\Delta m_{\gamma}}{\rho^{2}}\right]$$
$$\times\,\hat{e}^{*}_{\gamma'(\rho,z)}\cdot\hat{e}_{\gamma}(\rho,z)e^{-j(m'_{\gamma}-m'_{\gamma'})\phi}\rho\,d\rho\,dz\,d\phi. \tag{12}$$

The coefficient's vector $\vec{a}=[a_{1},a_{2},\ldots,a_{N}]^{T}$ has nonzero values only for a discrete number of wavelength λ_{l} where the corresponding determinant of the matrix is zero. The corresponding eigenvector gives the complex amplitudes a_{γ} in Eq. (5) and determines the field profile of the mode. We normalize these amplitudes according to

$$\sum_{\gamma=1}^{N}|a_{\gamma}|^{2}=1(J). \tag{13}$$

A. Quality factor estimation

Since, under the current formalism, the resulting perturbed field is the superposition of unperturbed WGMs, therefore, the power coupled to the fiber cannot be derived directly from the field pattern. Instead, the total quality factor (Q_{t}) has to be derived from a separate estimation of intrinsic Q (Q_{i}) and coupling Q (Q_{c}). Note

$$\frac{1}{Q_{t}}=\frac{1}{Q_{i}}+\frac{1}{Q_{c}}=\frac{P_{\text{abs}}+P_{\text{rad}}}{\omega\times U_{\text{cav}}}+\frac{P_{\text{coupling}}}{\omega\times U_{\text{cav}}}, \tag{14}$$

where U_{cav} is the total energy stored in the cavity and P_{abs}, P_{rad}, and P_{coupling} are the power lost through absorption, radiation, and coupling to the fiber. Here we ignore the scattering-induced loss, which can be estimated through Mie or Rayleigh scattering theory if the surface roughness and cavity material defects distributions are known [33,34]. In this case, the polygon field pattern obtained in our method can be used for such a calculation. Additionally, one may also incorporate the scattering loss as part of the imaginary part of the cavity refractive index, in which case the intrinsic Q obtained in our model will automatically include scattering induced Q. P_{abs}, P_{rad}, and the resulting Q_{i} can be estimated from the field distributions (see details in Supplemental Material, Sec. S.2 [16]). Alternatively, since the polygon mode is a linear combination of unperturbed whispering gallery modes (WGMs) in the absence of the coupling loss, Q_{i} can also be derived from the complex resonance wavelength λ_{l} in Eq. (11)

$$Q_{i}=\frac{\text{Re}\{\lambda_{l}\}}{2\text{Im}\{\lambda_{l}\}}. \tag{15}$$

To estimate the coupling loss, the coupled mode theory (CMT) needs to be used [35]. Assuming a Cartesian coordinate system (x',y',z') for the fiber with $\hat{z}'$ the direction of propagation as shown in Fig. 1, the fiber field can be written as

$$\vec{E}_{f}(x',y',z')=b(z')\hat{e}_{f}(x',y'),$$
$$\vec{H}_{f}(x',y',z')=b(z')\hat{h}_{f}(x',y'). \tag{16}$$

Here, the fiber electric and magnetic mode field distributions $\{\hat{e}_{f}(x',y'),\hat{h}_{f}(x',y')\}$ are normalized such that the power propagating along the z' direction is $|b(z')|^{2}$. As $b(-\infty)=0$, $b(+\infty)$ only contains the field coupled to the fiber output from the cavity [30,36], we have

$$|b(z')|^{2}=\left|\frac{k_{0}}{4\eta_{0}}\int_{-\infty}^{z'}dz''\iint\vec{E}(x'',y'',z'')\right.$$
$$\left.\cdot\,[\Delta\tilde{\epsilon}_{f,r}\hat{e}^{*}_{f}(x'',y'')]e^{j\beta_{f}z''}dA\right|^{2}, \tag{17}$$

where β_{f} is the propagation constant for the fiber mode. Coupling loss then can be derived from $P_{\text{coupling}}=|b(+\infty)|^{2}$. A detailed discussion on coupling the Q calculation can be found in the Supplemental Material, Sec. S.3 [16].

B. 2 + 1-D simplification

Under 2-D approximation by using the effective index method to reduce the three-dimensional photonic structure to a two-dimensional one with the refractive index profile invariant along the $\hat{z}$ direction ($\frac{\partial}{\partial z}\equiv 0$), WGMs decouple to $\hat{z}$-independent TE and TM modes with nonzero field profiles $\{e_{\gamma,z}(\rho),h_{\gamma,\rho}(\rho),h_{\gamma,\phi}(\rho)\}$ and $\{h_{\gamma,z}(\rho),e_{\gamma,\rho}(\rho),e_{\gamma,\phi}(\rho)\}$, respectively. The polygon and star modes can still be obtained following the formalism above except that the matrix elements in Eq. (12) should be obtained from

$$\Lambda_{\gamma'\gamma}=\int_{\phi=0}^{2\pi}\int_{\rho=0}^{\infty}\left[2\epsilon_{r}(\rho,z)k_{\gamma}\Delta k_{\gamma}+k_{\gamma}^{2}\Delta\epsilon_{r}(\rho,\phi)\right.$$
$$\left.-\frac{2m_{\gamma}\Delta m_{\gamma}}{\rho^{2}}\right]\hat{e}^{*}_{\gamma'}(\rho)\cdot\hat{e}_{\gamma}(\rho)e^{-j(m'_{\gamma}-m'_{\gamma'})\phi}\rho\,d\rho\,d\phi. \tag{18}$$

Since the variations in the z direction are mapped to the 2-D problem, we call this method 2 + 1-D simplification. In general, the 2-D WGM field profiles can be obtained numerically

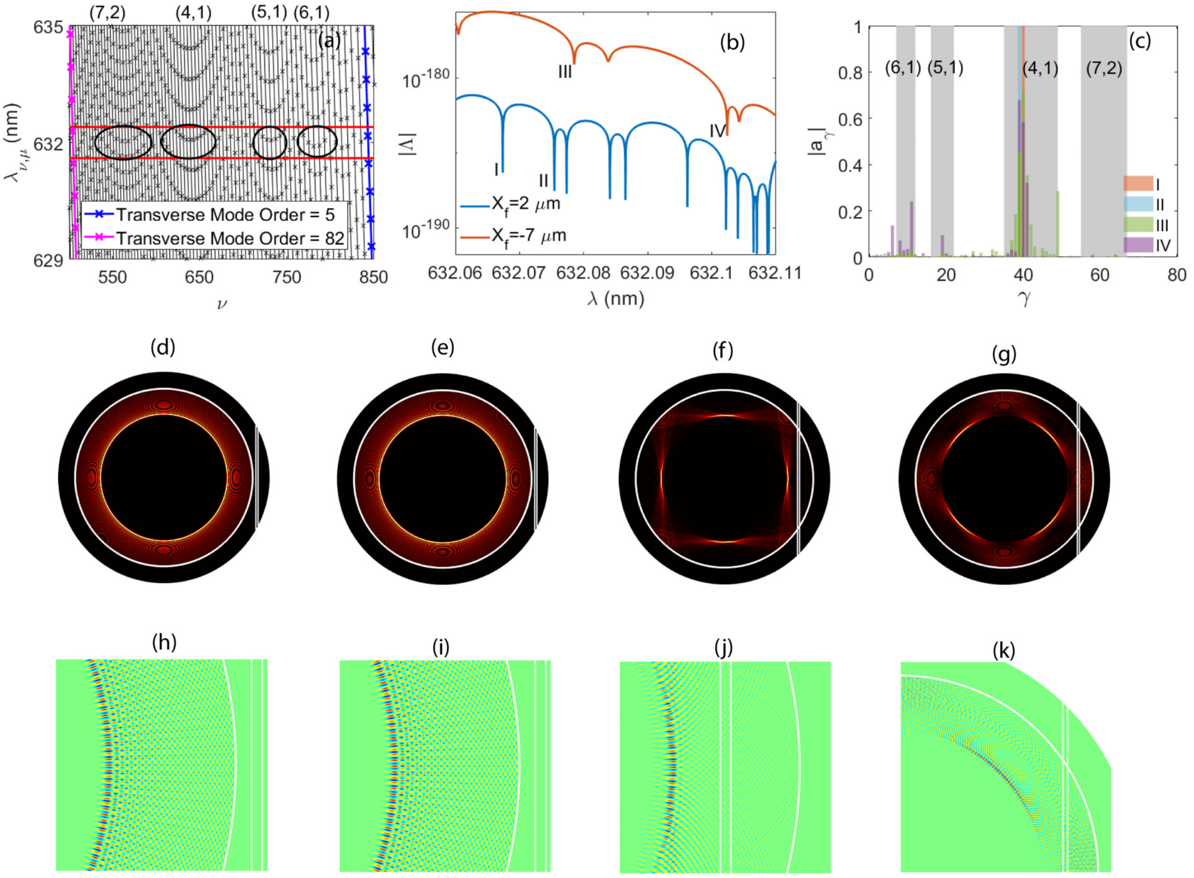

FIG. 2. (a) The resonance wavelengths of TE WGMs at different azimuth mode orders ν. Black lines connect the same transverse mode order μ. Transverse mode orders of 5 and 82 are shown with pink and blue lines. Subsets of WGMs with (p, q) pairs of (7,2), (4,1), (5,1), and (6,1) are shown in the figure with black circles. (b) The determinant $|\det(\tilde{\Lambda})|$ in the range [632.05,632.11] nm. For the first case (orange line), $X_f = -7$ µm and for the second case (blue line), $X_f = 2$ µm. (c) The amplitudes $|a_\gamma|$ for the modes I to IV in labeled in subplot (b). (d)–(g) The intensity profiles of the modes. (h)–(k) The zoom-in plots of electric field profiles E_z for each mode.

according to

$$\frac{1}{\rho}\frac{\partial}{\partial\rho}\left(\rho\frac{\partial}{\partial\rho}\right)\hat{e}_{\nu\mu}(\rho)+\left[\epsilon_r(\rho)k_{\nu\mu}^2-\frac{m_{\nu\mu}^2}{\rho^2}\right]\hat{e}_{\nu\mu}(\rho)=\vec{0},$$
$$\frac{1}{\rho}\frac{\partial}{\partial\rho}\left(\rho\frac{\partial}{\partial\rho}\right)\hat{h}_{\nu\mu}(\rho)+\left[\epsilon_r(\rho)k_{\nu\mu}^2-\frac{m_{\nu\mu}^2}{\rho^2}\right]\hat{h}_{\nu\mu}(\rho)=\vec{0}. \tag{19}$$

In the special case where the wedge angle $\theta_w = 90^\circ$, the analytic solution is obtainable [27] as shown in the Supplemental Material Sec. S.4 [16]. In this case, Eq. (18) can be solved through the analytical mode solution efficiently.

III. RESULTS AND DISCUSSION

A. 2 + 1-D perturbation results

We first model polygon modes under the 2-D approximation and assume the wedge angle $\theta_w = 90^\circ$ so that the analytical solution of WGMs can be adopted. The disk geometry is identical to the actual disk demonstrated in [14] with $R = 42$ µm, $t = 700$ nm, $d = 0$ nm and at wavelengths around 632 nm. The ordinary and extraordinary refractive index of LN is set to $n_e = 2.2033$ and $n_o = 2.287$. The imaginary parts of both refractive indices are calculated from $\kappa = \frac{\lambda\alpha}{4\pi}$, where $\alpha = 0.0019\,\mathrm{cm}^{-1}$ is the linear absorption coefficient [37]. Figure 2(a) shows the resonance wavelengths of unperturbed TE WGMs as a function of the azimuthal mode order ν. Straight lines connect the modes with the same transverse mode order μ. In particular, $\mu = 5$ and $\mu = 82$ are shown as blue and pink lines in the plot and the black lines between them correspond to modes with μ in between. The WGMs with azimuthal and transverse mode orders of $\nu(n) = \nu_0 + n \times p$ and $\mu(n) = \mu_0 - n \times q$ are nearly degenerate for (p, q) pairs of (7,2), (4,1), (5,1), and (6,1) at the subsets shown within the black ellipse in Fig. 2(a). Here, n is an integer and ν_0 and μ_0 are the azimuthal and transverse mode order of the first member in the subset. The near degeneracy of certain subsets of WGMs would lead to solutions for which the only nonnegligible coefficients in Eq. (5) belong to this subset. The shape of the resulting polygon or star mode then can be predicted from the (p, q) pair. p shows the number of bouncing points along the boundary and q shows the number of windings until we return to the initial point [27]. Therefore, the subsets with $q = 1$ correspond to polygon modes and the subsets with $q > 1$ correspond to star modes.

In general, to find the mode of a particular polygon shape, it is sufficient to select the WGMs of the corresponding

(p, q) pairs within the black circle in Fig. 2(a). Here, for demonstration purposes, we select all the 79 WGMs whose transverse mode orders are between 5 and 82, and resonance wavelengths within one mean free spectral range (FSR, 0.8 nm) of the center wavelength [632 ± 0.4 nm, shown between the horizontal red lines in Fig. 2(a)]. These modes are inserted into Eq. (5) for two different cases. In the first case, fiber is placed on top of the microdisk with $X_f = -7$ µm and in the second case, fiber is placed far away from the microdisk with $X_f = +2$ µm. Figure 2(b) shows the determinant $|\tilde{\Lambda}|$ versus λ_l for both cases. As shown, a set of dips can be found in both the first case (orange solid line) and the second case (blue solid line). Each dip represents a resonant mode of the perturbed cavity since $|\tilde{\Lambda}| = 0$ leads to nonzero solutions to $\vec{a}$ that are the coefficients of the contributing WGMs coherently forming the resonance mode. Here, we selected two modes in each case and labeled them by I to IV on the plot for further investigation.

The WGMs amplitudes $|a_\gamma|$ for all the four labeled modes are shown in Fig. 2(c). In the second case where $X_f = +2$ µm, the coupling quality factor, Q_c for modes I and II are 5.5×10^{20} and 1.4×10^{21}, indicating a weak interaction between the fiber and disk. Consequently, only one nonzero a_γ is present for mode I (orange bar) and mode II (blue bar), leading to pure WGM modes as shown from the intensity distributions in Figs. 2(d) and 2(e) since the perturbation is too weak to excite multiple WGMs. For $X_f = -7$ µm where the perturbation is relatively strong, the Q_c of modes III and IV are 7.2×10^8 and 2×10^8, respectively. With such strong fiber-to-disk interactions, there are multiple nonzero a_γ values that coherently combine the WGMs into a polygon as shown in Figs. 2(f) to 2(g). The intensity of these modes is shown in Figs. 2(d) to 2(g) with the corresponding zoom-in images of electric field distributions in Figs. 2(h) to 2(k). For the square modes III and IV, the nonzero amplitudes around $\nu = 40$ correspond to the subset with $(p, q) = (4, 1)$. The total quality factor Q_t for modes I to IV are 1.1×10^8, 1.1×10^8, 9.6×10^7, and 7.1×10^7, respectively.

To obtain polygon and star modes of different shapes, we placed the fiber at different X_f with fiber in direct contact with the disk top ($d = 0$). As shown in Fig. 3(a), when X_f is at -7 µm, two modes were observed at resonance wavelengths λ_l of 632.0838 nm and 632.0107 nm and labeled as I and II. The significant values of $\vec{a}$ fall into $(p, q) = (4, 1)$ and (6,1), respectively, suggesting the creation of square and hexagon modes. The top view intensity profiles showing as the insets in Fig. 3(b) confirmed that these two modes are the shapes suggested. We further placed the fiber at $X_f = -2$ µm to find a pentagon mode (III) at $\lambda_l = 632.067$ nm with $(p, q) = (5, 1)$. Finally, a heptagram mode (IV) was located at $X_f = -1$ µm with $(p, q) = (7, 2)$ and $\lambda_l = 632.0627$ nm, both of which are also confirmed by the insets in Fig. 3(b). The main plot of Fig. 3(b) further shows the optical power coupled to the fiber ($|b(z')|^2$) for these modes. The coupling Q calculated for the modes I to IV based on $b(+\infty)$ is 7.2×10^8, 2.5×10^9, 6.4×10^9, and 2.7×10^9, respectively. It is worth mentioning that for modes II and III, even though the fiber is placed in contact with the disk surface and the perturbation is strong, the overlap between the mode intensity to the fiber remains small. Consequently, the coupling loss is low, making a high overall quality factor possible. In contrast, a normal WGM would have low coupling Q due to overcoupling when the fiber is at the same location. Our simulation results further confirm the experiment observation in [14,15] that a polygon mode may have a high Q_t even when the fiber is placed on the disk top.

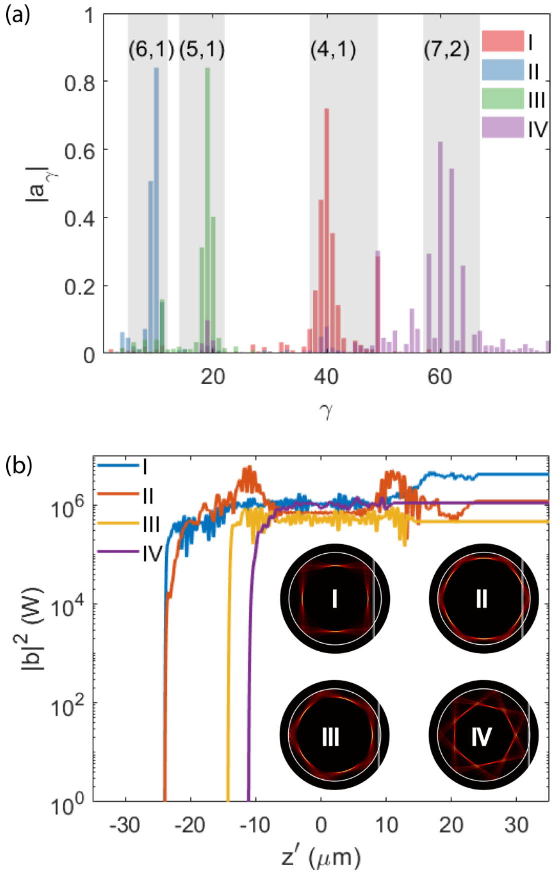

FIG. 3. (a) $|a_\gamma|$ of the square (I), hexagon (II), pentagon (III), and heptagram (IV) modes when $X_f = -7$ µm for I and II, while $X_f = -2$ µm for III and $X_f = -1$ µm for IV. (b) Optical power ($|b(z')|^2$) propagating along the tapered fiber in the absence of light from its input end. Insets are the top-view intensity profiles of these modes. The coupling Q of these modes are 7.2×10^8, 2.5×10^9, 6.4×10^9, and 2.7×10^9, respectively.

B. 3-D perturbation results

In this subsection, we apply the 3-D full vector perturbation to polygon mode analysis. Here, we adopt a disk similar to the one that has been experimentally demonstrated in [15] with $R = 14.53$ µm, $t = 700$ nm, a wedge angle $\theta_w = 61.6^\circ$, and at wavelengths around 970 nm. The ordinary and extraordinary refractive index and linear absorption coefficient of LN are set to $n_e = 2.1615$, $n_o = 2.2385$. As the absorbance of the crystal is supplier dependent and the value of thin film used in [14,15] is not available, we use $\alpha = 0.0019\,\text{cm}^{-1}$ according to [37]. The fiber has a diameter of 600 nm centered at $X_f = -2.53$ µm. The vertical gap between the fiber and the microdisk is $d = 150$ nm. In total, we illustrated three modes by sweeping the wavelength from 972.39 nm to 972.53 nm

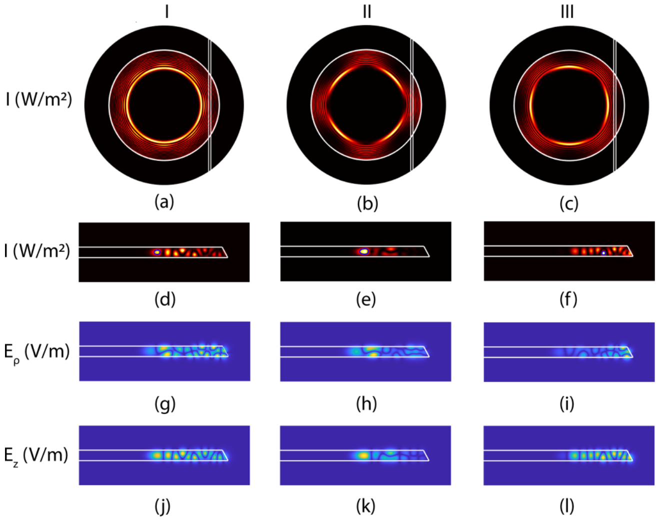

FIG. 4. The top view intensity profile at $z = 0$ of (a) star mode, (b) square mode at 45°, and (c) horizontal square mode. Their resonant wavelength and quality factor (λ_l, Q) are (972.4097 nm, 7.1×10^7), (972.4165 nm, 4.6×10^6), and (972.4314 nm, 2.1089×10^6), respectively. The intensity (I), electrical field along radial (E_ρ), and vertical (E_z) at $\phi = 45^\circ$ are displayed in (d)–(f), (g)–(i), and (j)–(l).

and labeled them as I, II, and III in Fig. 4. The top-view intensity profiles of these modes at $z = 0$ cross section in Figs. 4(a) to 4(c) show that mode I is a weakly formed star mode while modes II and III are square modes, one oriented 45° from $\hat{x}$ while the other is horizontal. The side-view at $\phi = 45^\circ$ of intensity (I), electrical fields along radial (E_ρ), and vertical (E_z) directions are shown on Figs. 4(d) to 4(f), 4(g) to 4(i), and 4(j) to 4(l), respectively. The total quality factor (Q_t) for the modes I to III are 7.1×10^7, 4.6×10^6, and 2.1×10^6, respectively. A video showing the 3-D field distribution is available in the Supplemental Material.

C. Comparison between 2 + 1-D and 3-D approaches

To compare with 2 + 1-D perturbation method, we further investigate the polygon mode evolution by varying the slant wedge angle θ_w and setting $d = 200$ nm.

In 2 + 1-D perturbation, the analytic solution of 2-D WGMs is no longer available due to the appearance of the slant wedge angle and we adopted the numeric solution through COMSOL instead to obtain the WGMs (see Supplemental Material Sec. S.5 [16]). To evaluate the quality of the square mode, we defined a visibility V_{2d} at $\phi = 45^\circ$ according to

$$V_{2d} = \frac{\int_{\rho_{h1}}^{\rho_{h2}} I(\rho, \phi = 45^\circ) d\rho}{\int_{-\infty}^{\infty} I(\rho, \phi = 45^\circ) d\rho}. \tag{20}$$

Here ρ_{h1} and ρ_{h2} are the locations of the full width at half maximum (FWHM) of the mode intensity $I(\rho, \phi = 45^\circ)$ at $\phi = 45^\circ$. In this simulation, we sweep the wedge angle from 57° to 80° to obtain a resonant mode at each angle. Using a Windows-10 computer with single Intel i7-7700K CPU operating at 4.20GHz and 64 GB memory, it takes around 850 seconds to obtain each resonant mode. Shown as the red curve in Fig. 5(a), the resonance modes are WGM in nature when we start to increase θ_w till 76°, as evident from the top-view intensity profile below the main plot (II). When the wedge angle reaches 77°, a sharp rise of visibility to 0.4 suggests the formation of a square mode, which is confirmed by the intensity profile (I).

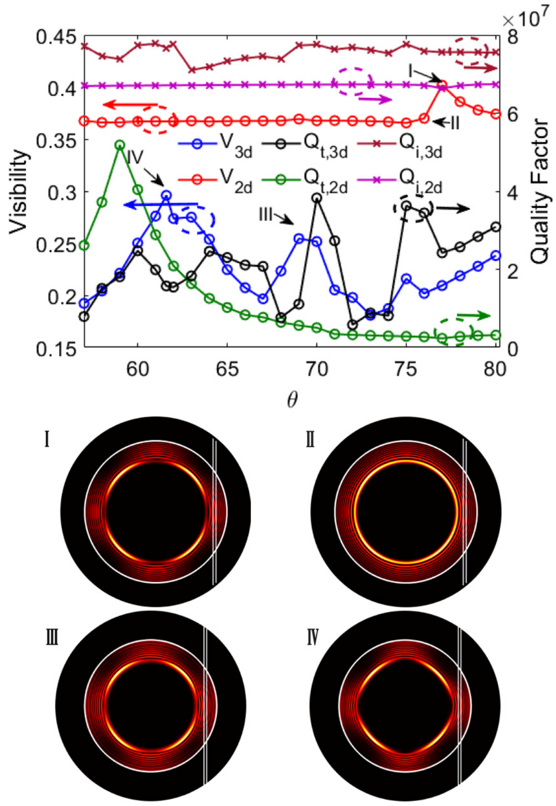

FIG. 5. Top: Visibility (V), intrinsic quality factor (Q_i), and total quality factor (Q_t) as a function of wedge angle calculated for the same structure using 2 + 1-D and 3D methods. Bottom: Intensity distribution top-view of modes I, II, III, and IV labeled in the top plot.

In 3-D, similar to the 2 +1-D case, we define a 3-D visibility V_{3d} of the square modes as

$$V_{3d} = \frac{\iint_{S_h} I(\rho, z, \phi = 45^\circ) d\rho dz}{\int_{-\infty}^{\infty}\int_{-\infty}^{\infty} I(\rho, z, \phi = 45^\circ) d\rho dz}. \tag{21}$$

Here, $I(\rho, z, \phi)$ is the intensity profile and S_h is the area where the intensity is above the half maximum intensity. Similarly, we perform a wedge angle sweep to compute the resonant modes accordingly. Using the same computer, the computation of each mode takes around 5,700 seconds. In this simulation, we observe two clear polygon modes with high visibility at $\theta = 61.6^\circ$ and $\theta = 67^\circ$. The higher visibility at $\theta = 61.6^\circ$ is due to the fact that the resonance wavelengths of the contributing WGMs are closer (see Supplemental Material Sec. S.6 [16]). Note that the large departure of the wedge angle between the 2 + 1-D and 3-D simulation suggests that although 2 + 1-D is a fast algorithm with reasonable accuracy in generating field patterns, it is less accurate in the presensce of highly sensitive parameters such as the wedge angle. A video showing the polygon mode evolution versus the wedge angle is available in the Supplemental Material.

Further, we compare the intrinsic Q (pink curve with cross markers for $2+1$-D and brown curve with cross markers for 3-D) and total Q (green curve with circle markers for $2+1$-D and black curve with circle markers for 3-D) in Fig. 5(a). As shown, in our $2+1$-D model, Q_i varies around $(6.6 \sim 6.7) \times 10^7$ and Q_t around $(0.3 \sim 5.1) \times 10^7$, both with relatively smooth changes with wedge angle. In contrast, our 3-D model shows that Q_i is around $(7.2 \sim 7.8) \times 10^7$ and Q_t around $(0.8 \sim 3.8) \times 10^7$. Our $2+1$-D and 3-D results agree quite well even though the effective index method is known to be less accurate to capture the field fluctuation along $\hat{z}$. On the other hand, the relatively rich fluctuations of Q versus wedge angle in our 3-D simulation indicate that the 3-D model has higher sensitivity and accuracy to take the vertical light confinement into account.

In the next comparison, we study the evolution of the polygon modes by varying the fiber-to-disk distance d, with the wedge angle in $2+1$-D and 3-D simulations set at each of their optimum value (77° for $2+1$-D and 61.6° for 3-D). Further, we optimize the $X_f = -1.33\ \mu\text{m}$ in $2+1$-D simulation so that the visibility reaches the highest. Figure 6(a) shows Q_t (blue curve with cross markers to the left axis), Q_c (green curve with diamond markers), Q_i (black dashed line), and V_{2d} (yellow curve with plus markers to the right axis) versus d. The right inset of the intensity distribution at $d = 325$ nm indicates that when the gap between the fiber and the disk top is larger than a half wavelength, the perturbation is negligible and only WGM can be formed with a poor square mode visibility of 0.36. The mode also has an $Q_i = 6.8 \times 10^7$, $Q_c = 9.7 \times 10^7$, and a total quality factor $Q_t = 4{\times}10^7$, indicating that the fiber is at an undercoupled regime. When the fiber moves closer to the disk top with decreasing d, the resonance mode gradually evolves to the square mode with increasing visibility till reaches the best square shape at = 75 nm (left inset) at a resonance wavelength of 971.4453 nm and with visibility of 0.6 as a result of increased perturbation. On the other hand, due to the increased power coupling to the fiber, both Q_c and Q_t drop to 3.6×10^5, indicating that the fiber is at the overcoupled regime.

Figure 6(b) displays the 3-D simulation on intrinsic, coupling, and total quality factors and visibility evolution. According to the visibility curve (yellow line with plus markers), the sharpest square mode occurs at $d = 150$ nm with an Q_i (black dashed line and circle markers) of $7.7{\times}10^7$, Q_c (green line with diamond markers) of 4.9×10^6, and Q_t (blue line with cross markers) of 4.6×10^6. The d for the best visibility is almost twice as far as the $2+1$-D case, confirming that, although $2+1$-D perturbation provides fast modeling of the cavity polygon modes, it cannot accurately predict the exact wedge angle and fiber position as these parameters are sensitive to vertical light confinement. Further, the plot of 3-D Q_c and Q_t shows a "shoulder" pattern at d around 250 nm to 300 nm, which is also visible in $2+1$-D at a lower d. This is caused by the loss redistribution when the mode transits from a single WGM to multiple WGMs for polygon mode formation. It is also worth mentioning that the intrinsic Q obtained from Eq. (14) (black circles) and Eq. (15) (black dashed line) reach excellent agreement, indicating that both can be used for Q_i estimation. Further, we compared our 3-D simulation result with the measured Q_t reported in [15]. Although the surface roughness-induced scattering loss and precise fiber location of the disk reported in [15] were not known due to the resource limitation, the experiment result of $Q_t = 2.2 \times 10^7$ shown as the red dashed line is in line to our simulation at good visibility.

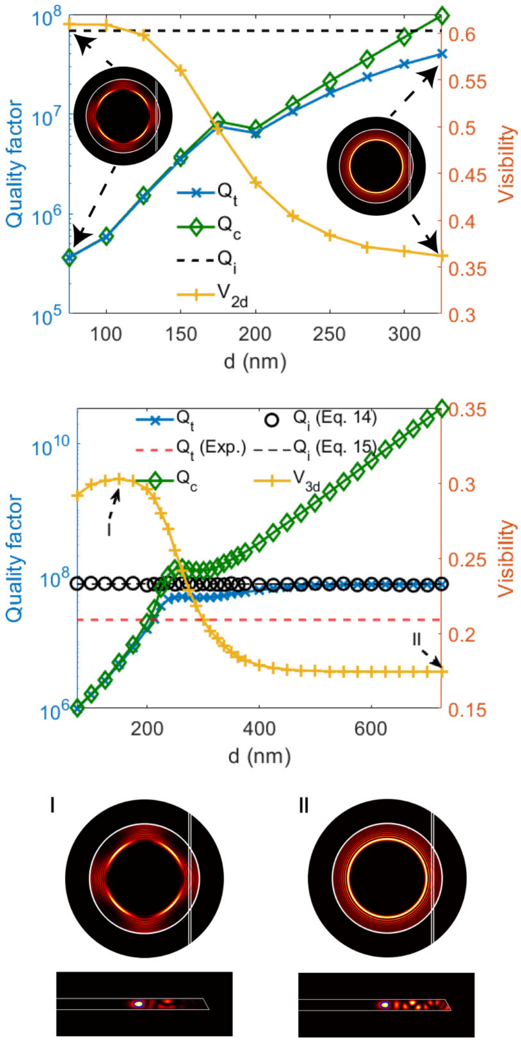

FIG. 6. (a) $2+1$-D simulation shows the intrinsic, coupling, and total quality factors and visibility evolution versus d. The disk wedge angle is 77°. The black dashed line shows the intrinsic quality factor (Q_i) when d is sufficiently large. The left inset is the intensity distribution of the square mode with the highest visibility of 0.6 and $Q_t = 3.6{\times}10^5$ at $d = 75$ nm while the right inset displays the intensity distribution of the WGM at $d = 325$ nm with $V_{2d} = 0.36$ and $Q_t = 4{\times}10^7$. (b) 3-D simulation of a structure identical to (a) except for a wedge angle of 61.6°. The dashed black line shows the (Q_i) calculated from Eq. (14) and the circles are those from Eq. (15) The top-view and side-view intensity profiles are also shown at $d = 150$ nm (I) and $d = 725$ nm (II). The experimentally measured total Q in [15] is shown as the red dashed line.

IV. CONCLUSION

In conclusion, through numerical analysis with $2+1$-D and 3-D perturbation methods, we confirmed that the polygon and star modes experimentally observed in [14,15] ewre due to fiber-induced perturbation. We further verified our experimental observation that the polygon modes may reach high overall quality factors even with the fiber placed close to the disk surface, which in general will cause overcoupling for conventional WGM. Furthermore, although the $2+1$-D perturbation method is a fast algorithm and provides reasonable accuracy in predicting field distribution and quality factors, it is less accurate in estimating parameters such as wedge angle and fiber-to-disk distance, which are highly sensitive to vertical light confinement. Under these situations, a more accurate 3-D perturbation approach is recommended.

[1] K. J. Vahala, Optical microcavities, Nature (London) **424**, 839 (2003).

[2] T. Lu, H. Lee, T. Chen, S. Herchak, J.-H. Kim, S. E. Fraser, R. C. Flagan, and K. Vahala, High sensitivity nanoparticle detection using optical microcavities, Proc. Natl. Acad. Sci. USA **108**, 5976 (2011).

[3] M. D. Baaske, M. R. Foreman, and F. Vollmer, Single-molecule nucleic acid interactions monitored on a label-free microcavity biosensor platform, Nat. Nanotechnol. **9**, 933 (2014).

[4] T. J. Kippenberg, R. Holzwarth, and S. A. Diddams, Microresonator-based optical frequency combs, Science **332**, 555 (2011).

[5] T. J. Kippenberg and K. J. Vahala, Cavity optomechanics: Backaction at the mesoscale, Science **321**, 1172 (2008).

[6] S. Honari, S. Haque, and T. Lu, Fabrication of ultra-high q silica microdisk using chemo-mechanical polishing, Appl. Phys. Lett. **119**, 031107 (2021).

[7] W. Yu, W. C. Jiang, Q. Lin, and T. Lu, Cavity optomechanical spring sensing of single molecules, Nat. Commun. **7**, 12311 (2016).

[8] B. Redding, L. Ge, Q. Song, J. Wiersig, G. S. Solomon, and H. Cao, Local Chirality of Optical Resonances in Ultrasmall Resonators, Phys. Rev. Lett. **108**, 253902 (2012).

[9] W. Fang, H. Cao, and G. S. Solomon, Control of lasing in fully chaotic open microcavities by tailoring the shape factor, Appl. Phys. Lett. **90**, 081108 (2007).

[10] J. Unterhinninghofen, J. Wiersig, and M. Hentschel, Goos-hänchen shift and localization of optical modes in deformed microcavities, Phys. Rev. E **78**, 016201 (2008).

[11] T. Harayama, S. Sunada, and K. S. Ikeda, Theory of two-dimensional microcavity lasers, Phys. Rev. A **72**, 013803 (2005).

[12] J. Wiersig and M. Hentschel, Combining Directional Light Output and Ultralow Loss in Deformed Microdisks, Phys. Rev. Lett. **100**, 033901 (2008).

[13] N. B. Rex, H. E. Tureci, H. G. L. Schwefel, R. K. Chang, and A. D. Stone, Fresnel Filtering in Lasing Emission from Scarred Modes of Wave-Chaotic Optical Resonators, Phys. Rev. Lett. **88**, 094102 (2002).

[14] Z. Fang, S. Haque, S. Farajollahi, H. Luo, J. Lin, R. Wu, J. Zhang, Z. Wang, M. Wang, Y. Cheng *et al.*, Polygon Coherent Modes in a Weakly Perturbed Whispering Gallery Microresonator for Efficient Second Harmonic, Optomechanical, and Frequency Comb Generations, Phys. Rev. Lett. **125**, 173901 (2020).

[15] J. Lin, S. Farajollahi, Z. Fang, N. Yao, R. Gao, J. Guan, L. Deng, T. Lu, M. Wang, H. Zhang *et al.*, Electro-optic tuning of a single-frequency ultranarrow linewidth microdisk laser, Adv. Photonics **4**, 036001 (2022).

[16] See Supplemental Material at http://link.aps.org/supplemental/10.1103/PhysRevA.108.033520 for an estimation of the intrinsic quality factor from the field distribution; derivation for coupling quality factor; analytical solution of 2-D WGM; the effective index method; and WGMs used in 3-D perturbation modeling. See also Refs. [27,31,32,36].

[17] S.-Y. Lee, S. Rim, J.-W. Ryu, T.-Y. Kwon, M. Choi, and C.-M. Kim, Quasiscarred Resonances in a Spiral-Shaped Microcavity, Phys. Rev. Lett. **93**, 164102 (2004).

[18] J. Wiersig, Boundary element method for resonances in dielectric microcavities, J. Opt. A: Pure Appl. Opt. **5**, 53 (2003).

[19] C.-L. Zou, Y. Yang, Y.-F. Xiao, C.-H. Dong, Z.-F. Han, and G.-C. Guo, Accurately calculating high quality factor of whispering-gallery modes with boundary element method, J. Opt. Soc. Am. B **26**, 2050 (2009).

[20] C.-L. Zou, H. G. Schwefel, F.-W. Sun, Z.-F. Han, and G.-C. Guo, Quick root searching method for resonances of dielectric optical microcavities with the boundary element method, Opt. Express **19**, 15669 (2011).

[21] I. Teraoka, S. Arnold, and F. Vollmer, Perturbation approach to resonance shifts of whispering-gallery modes in a dielectric microsphere as a probe of a surrounding medium, J. Opt. Soc. Am. B **20**, 1937 (2003).

[22] S. Arnold, M. Khoshsima, I. Teraoka, S. Holler, and F. Vollmer, Shift of whispering-gallery modes in microspheres by protein adsorption, Opt. Lett. **28**, 272 (2003).

[23] I. Teraoka and S. Arnold, Theory of resonance shifts in te and tm whispering gallery modes by nonradial perturbations for sensing applications, J. Opt. Soc. Am. B **23**, 1381 (2006).

[24] M. R. Foreman and F. Vollmer, Theory of resonance shifts of whispering gallery modes by arbitrary plasmonic nanoparticles, New J. Phys. **15**, 083006 (2013).

[25] J. D. Swaim, J. Knittel, and W. P. Bowen, Detection limits in whispering gallery biosensors with plasmonic enhancement, Appl. Phys. Lett. **99**, 243109 (2011).

[26] H. M. Lai, P. T. Leung, K. Young, P. W. Barber, and S. C. Hill, Time-independent perturbation for leaking electromagnetic modes in open systems with application to resonances in microdroplets, Phys. Rev. A **41**, 5187 (1990).

[27] J. Lee, S. Rim, J. Cho, and C.-M. Kim, Resonances near the Classical Separatrix of a Weakly Deformed Circular Microcavity, Phys. Rev. Lett. **101**, 064101 (2008).

[28] H. Türeci, H. Schwefel, P. Jacquod, and A. D. Stone, Modes of wave-chaotic dielectric resonators, in *Progress in Optics* (Elsevier, Amsterdam, 2005), pp. 75–137.

[29] N. Korneev, Perturbation approximation for higher modes in nearly regular two-dimensional cavities, Cogent Physics **3**, 1262725 (2016).

[30] M. L. Gorodetsky and V. S. Ilchenko, Optical microsphere resonators: Optimal coupling to high-q whispering-gallery modes, J. Opt. Soc. Am. B **16**, 147 (1999).

[31] X. Du, S. Vincent, and T. Lu, Full-vectorial whispering-gallery-mode cavity analysis, Opt. Express **21**, 22012 (2013).

[32] X. Du, S. Vincent, M. Faucher, M.-J. Picard, and T. Lu, Generalized full-vector multi-mode matching analysis of whispering gallery microcavities, Opt. Express **22**, 13507 (2014).

[33] M. Borselli, T. Johnson, and O. Painter, Beyond the Rayleigh scattering limit in high-Q silicon microdisks: Theory and experiment, Opt. Express **13**, 1515 (2005).

[34] M. Borselli, K. Srinivasan, P. E. Barclay, and O. Painter, Rayleigh scattering, mode coupling, and optical loss in silicon microdisks, Appl. Phys. Lett. **85**, 3693 (2004).

[35] D. Rowland and J. Love, Evanescent wave coupling of whispering gallery modes of a dielectric cylinder, IEE Proc. J Optoelectron. UK **140**, 177 (1993).

[36] A. W. Snyder and J. Love, *Optical Waveguide Theory* (Springer Science & Business Media, New York, 2012).

[37] D. N. Nikogosyan, *Nonlinear Optical Crystals: A Complete Survey* (Springer Science & Business Media, New York, 2006).